Predictable changes in extreme sea levels and coastal flood risk due to nodal and perigean astronomical tidal cycles

Alejandra R. Enriquez[1], Thomas Wahl[1], Hannah E. Baranes[2], Stefan A. Talke[3], Philip M. Orton[4], James F. Booth[5], Ivan D. Haigh[6]

[1]Department of Civil, Environmental and Construction Engineering and National Center for Integrated Coastal Research, University of Central Florida, Orlando, FL 32186, USA.

[2]Gulf of Main Research Institute, Portland, Main, USA

[3]Department of Civil and Environmental Engineering, California Polytechnic State University, San Luis Obispo, CA 93407, USA

[4]Oceanography Department, Stevens Institute of Technology, Hoboken, NJ, USA

[5]Earth and Atmospheric Sciences, City College of New York, and Earth and Environmental Science, The Graduate Center, City University of New York, New York, NY, 10016, USA

[6]School of Ocean and Earth Science, National Oceanography Centre Southampton, University of Southampton, Waterfront Campus, European Way, Southampton SO14 3ZH, UK

Corresponding author: Alejandra R. Enriquez (`a.enriquez@ucf.edu`)

Key Points:

- 18.6-year nodal and 4.4-year perigee tidal cycles modulate extreme sea levels and affect estimates of flood risk
- The timing of the peak of the modulation is influenced by the relative importance of each cycle (nodal or perigee) over the total amplitude
- Tidally-induced changes in extreme sea levels affect estimates of total inundation area

Keywords: Nodal tide, perigean tide, flood mapping, flood hazard, extreme sea levels.

Abstract

We demonstrate that long-term tidally-induced changes in extreme sea levels affect estimates of major flood hazard in a predictable way. Long-term variations in tides due to the nodal and perigean tidal cycles influence extreme sea levels at 234 global tide gauges out of a total of 344. Results show regions where the amplitudes of the modulations are particularly relevant in the 100-year return sea level; the eastern coast of China, the northwestern and northeastern coasts of Australia, the northeast coast of Pacific, and the eastern coast of Europe, reaching up to ~22 cm in western France. We identify locations that are currently in a positive phase of the modulation and therefore at a higher risk of flooding,

as well as when (year) the next peak of the nodal/perigean modulations is expected to occur. The timing of the peak of the modulation is spatially coherent and influenced by the relative importance of each cycle (nodal or perigee) over the total amplitude. An evaluation of four locations suggests that the potentially flooded area in a 100-year event can vary up to ~45% (in Boston) as a result of the long-term tidal cycles; however, areal change is often smaller due to local topography and tidal characteristics (6-13%). We conclude that tidally-modulated changes in extreme sea levels can alter the potentially inundated area in a 100-year event and that the traditional, fixed 100-year floodplain is inadequate for describing coastal flood risk.

Plain Language Summary

Interannual and decadal (long-term) variations in tides modulate extreme sea levels, increasing the risk of flooding at specific and predictable times. Here, we use a dataset of 344 tide gauge to estimate the magnitude of the long-term tidally induced changes in extreme sea levels as well as to identify the timing of the peak of the modulations. We find significant amplitudes of the long-term tidal modulations in extreme water levels. The modulations are currently (in 2021) under a positive phase in the vast majority of places. We conclude that the long-term modulations in tides influences the total inundation area and, therefore, they should be taken into account when assessing coastal vulnerability.

1. Introduction

Flooding can severely impact coastal communities, producing large economic losses, damage to critical infrastructure, and casualties. In the United States (U.S.), annual damages caused by extreme sea levels typically exceed tens of billions of dollars (Kron, 2013) and they are expected to increase due to mean sea-level rise and the continued population growth along the coasts (Preston, 2013; Titus et al., 2009). Indeed, hurricane and flood losses, including riverine and coastal, have already tripled over the past fifty years (Gall et al., 2011). Local-scale flood mapping and vulnerability assessments are often developed to aid in adaptation planning (some examples are Gesch et al., 2020; Maloney and Preston, 2014; Rao et al., 2020; Ward et al., 2011). Such flood maps often determine land-use policies, flood mitigation strategies, and infrastructure development. In the U.S., the Federal Emergency Management Agency (FEMA) determines flood insurance requirements based on flood maps; owners, renters, and businesses in FEMA-designated zones with a 1% annual recurrence probability of flooding are required to purchase flood insurance on federally-backed loans. The coastal flood maps, however, sometimes underestimate the extent of the flood zone. In Fort Lauderdale, Florida, new estimates show that 64% of properties are at risk of flooding, in contrast to the 41% of properties included in FEMA's flood maps (Flavelle et al., 2020).

Coastal flood maps and hazard assessments in a regulatory framework, are typically developed under the assumption of stationarity. That is, all components of the water-level spectrum (mean sea level variability, astronomical tides, me-

teorologically induced storm surges, waves, etc.) are assumed to be unaffected by long-term trends or predictable cycles, after removing the effects of mean sea-level rise. However, astronomical tides are a quasi-deterministic part of measured water levels, and they strongly influence coastal water levels at daily, fortnightly, seasonal, interannual, and decadal time scales. Interannual and decadal (long-term) variations in tides mainly result from the 8.85-year perigean lunar cycle and 18.61-year lunar nodal cycle. The 8.85-year perigean lunar cycle is determined by the Moon's elliptical orbit around the Earth. The least distance between the Moon and the Earth is called perigee while the longest distance is known as apogee. The line that joins these two points in the space completes a full revolution in 8.85 years and influences high water levels at a period of 4.4-years (details in Section 3.4 and Ray and Merrifield (2019)). The nodal tide is produced by the relative movement of the plane in which the Moon orbits the Earth. This plane is inclined at 5° 09' to the plane of the ecliptic (the plane in which the Earth orbits the Sun) and rotates slowly over a period of 18.61-years, affecting the amplitude of the tides at the same frequency (Pugh and Woodworth, 2014).

Recent studies have shown that the nodal and perigean cycles can lead to more recurrent minor tidal flooding, resulting in substantial socio-economic disruptions and damages (Li et al., 2021; Ray and Foster, 2016; Thompson et al., 2021). The long-term tidal cycles have been also reported in high tide levels (sea levels of 1-year return period or less) at global scale either using numerical models (Haigh et al., 2011) or tide gauges observations (Menéndez and Woodworth, 2010; Peng et al., 2019). However, the nodal and perigean modulations in low-frequency extreme sea levels have been assessed regionally only. In the Gulf of Maine, U.S., the nodal cycle drives decadal-time scale variability in the 10- and 100-year flood levels at a rate exceeding the historical rate of sea-level rise (Baranes et al., 2020; Talke et al., 2018). Along the western Australian coast, the nodal and perigean amplitudes in the 0.5% annual exceedance tide levels can reach 7 and 9 cm, respectively (Eliot, 2010). Sobey (2005) also identified the nodal cycle in the 10-, 50-, and 100-year return sea levels at San Francisco tide gauge.

There are no studies that have assessed the nodal/perigean modulations in low-frequency, high impact extreme sea levels globally. Also, despite its importance and the relevance of flooding maps for coastal populations and risk management, there are no studies that have assessed how tidally-induced changes in extreme sea levels change potentially flooded surface area, and thus, the consequences for inundation go unaddressed. Here, we use the quasi-nonstationary skew surge joint-probability method (qn-SSJPM) of Baranes et al. (2020) to ask the question: how large are tidally-induced variations in flood hazard globally? and How important are these variations to flood inundation? We first obtain the nodal/perigean modulations in five tidal constituents (M_2, N_2, O_1, K_1, and S_2) at a global network of 344 tide gauges. Then, we analyze the amplitude and peak timing of the long-term tidally-induced changes in the annual 100-year return sea levels at the tide gauges. Finally, we assess the tidally-driven

variation in the spatial extent of flooding for four U.S. coastal cities; Boston (Massachusetts), Santa Barbara (California), Miami (Florida), and South San Francisco Bay (California), where high spatial resolution of digital elevation model (DEM) are available.

1. Data

Two main sources of data are used in this study: (1) water level records, and (2) elevation data. These are described in turn below.

1. Observed water levels

We use hourly water level observations from the Global Extreme Sea Level Analysis (GESLA-2; Woodworth et al., 2017). The GESLA-2 database contains 1,355 water level records with hourly or higher temporal frequency from tide gauges located along the global coasts. The tide gauge records in GESLA-2 are retrieved from a range of different sources, including the University of Hawaii Sea Level Center (UHSLC, Caldwell and Merrifield, 2015), the Japan Meteorological Agency (JMA), the National Tidal Centre Australia (NTCA), the National Oceanic and Atmospheric Administration (NOAA), and the British Oceanographic Data Centre (BODC), which provide most of the data sets. Tide gauge records in GESLA-2 have not been updated since 2017, but we updated records from some tide gauges for the present analysis, where possible. Out of the 1,355 records from the public and private GESLA-2 dataset, we select a subset of 344 records according to the following criteria:

1. Duplications: For some stations, the same water level information is retrieved from different providers, creating duplications. In such cases, we retain the longest record available. After removing duplicates, 854 time series remain.

2. Record length and completeness: Water level records are visually checked, and physically unrealistic jumps in water level are removed. Only years with at least 70% data completeness are analyzed. To evaluate the effect of the 18.61- and 8.85-year cycles, only stations with records lengths >30 years are used.

3. Three tide gauges located in Italy are removed due to sharp changes in the datum. These are the tide gauges at Bari, Catania, and Livorno.

4. Due to the high socio-economic development in the area, we also analyze the nodal/perigean tidal modulations in extreme sea levels as well as their influence on flood hazard in South San Francisco Bay, California. Water level observations at this location are retrieved from the Redwood City tide gauge record, which is part of the NOAA tide gauge dataset but not included in GESLA-2. The Redwood City record starts in 1973, but we have included only water level observations from 1997 to 2020 because of large gaps present in the pre-1977 records. Although the length of the Redwood water level time series is less than 30 years (23 years), we include it in the analysis due to its relevance to the neighboring area.

(a) **Digital elevation models**

Digital elevation models (DEM) for Santa Barbara, South San Francisco Bay, Boston, and Miami (U.S.) are based on high-resolution LiDAR data downloaded from the NOAA Digital Coast Data Access Viewer (NOAA, 2021). The name and resolution of the LiDAR dataset used in each study area as well as their horizontal resolution are shown in Table 1. Each LiDAR dataset is composed of several TIFF-format files, from which we only use those including topographic information along the coast. In the case of South San Francisco Bay, we reduce the horizontal point spacing from 0.7 cm (the original point LiDAR resolution) to 3 meters in order to alleviate the computational and time demand when performing the flooding maps (Section 3.5). The vertical datum of each LiDAR dataset is adjusted to reflect the datum (mean sea level) corresponding to the closest tide gauge included in our dataset (the datums used in the present study can be found in NOAA tide and currents[1]).

Table 1. Name and spatial resolution of the LiDAR datasets used in each study case.

Study area	**Lidar dataset**	**Spatial resolution (m)**
California	2002/2003 IfSAR data for Southern California	3
South San Francisco Bay	2010 USGS Lidar: San Francisco (CA)	3
Boston	2009 Boston & Cambridge (MA)	1
Miami	2018 Miami-Dade County ITD Lidar DEM	1.5

1. **Methods**

(a) **Tidal analysis and skew surge**

Water levels recorded at each tide gauge (Section 2.1) are the sum of mean sea level, astronomical tide, and the non-tidal residual (i.e., observed water level minus astronomical tide and mean sea level). Given that most cities and tide gauges are located inside estuaries and wave-sheltered embayments, the effect of wave breaking raising mean water levels has a minimal effect on the residual, and thus, we neglect this component.

We first remove the influence of mean sea level variation by subtracting a 12-month moving average from the hourly water level time series. Then, the tidal analysis is conducted independently for each calendar year. The predicted astronomical tide is estimated at each station using the MATLAB U-Tide harmonic analysis tool (Codiga, 2011). U-tide is applied using the least-squares method, white noise floor assumption for confidence intervals, and an automated choice of constituents resulting in 53 tidal constituents per year on average. We use a 369-day analysis period (12.5 lunar months) to consider a time span close to multiples of the synodic periods of the short-term tidal constituents. In order

[1]https://tidesandcurrents.noaa.gov/

to assess the influence of the nodal/perigean cycles in sea levels, the astronomical tides are calculated without nodal corrections; thus, it remains in the tidal constituents. We fit a 6-minute cubic spline function to the hourly measured water levels and predicted astronomical tide to reduce the peak truncation by the hourly time resolution (Baranes et al., 2020). We use skew surge levels to represent the non-tidal residual. Skew surge levels are calculated as the difference between the maximum observed high water (after detrending) and the maximum predicted astronomical tide in each tidal cycle, regardless of its timing.

1. **Nodal and perigean amplitudes in tidal constituents**

We estimate the amplitude of the nodal/perigean modulations for the following five main tidal constituents at each tide gauge (the maximum nodal/perigean modulations in the equilibrium theory are shown in brackets for each constituent): M_2 (3.7%), N_2 (3.7%), O_1 (18.7%), K_1 (11.5%), and S_2. The nodal/perigean cycles produce a negligible effect on the semi-diurnal solar S_2 constituent, however, noticeable variations in the S_2 amplitude at the period of the nodal cycle have been found in previous studies, mainly due to nonlinear interactions with M_2 (Ray and Talke, 2019), and hence it is included here.

A least-squares regression model is used to estimate the amplitudes of the nodal (18.61-years) and perigean (8.85-years) cycles for each tidal constituent as the expression:

$$H(t) = \beta_0 + \beta_1(t) + \beta_2 \cos\left(t * \tfrac{2\pi}{18.61}\right) + \ \beta_3 \sin\left(t * \tfrac{2\pi}{18.61}\right) + \ \beta_4 \cos\left(t * \tfrac{2\pi}{8.85}\right) \ + \beta_5 \sin\left(t * \tfrac{2\pi}{8.85}\right) \ (1)$$

where $H(t)$ is the annual value at the year t, β_0 is the constant value, and β_1 is the linear trend. β_2 and β_3 are the amplitudes of the cosine and sine functions of the 18.61-year nodal modulation and β_4 and β_5 of the 8.85-year perigean modulation. The amplitudes of the nodal (A_N) and perigean (A_P) modulations in each tidal constituent are computed as:

$$A_N = \ \sqrt{\beta_2^2 + \beta_3^2} \ (2)$$

$$A_P = \ \sqrt{\beta_4^2 + \beta_5^2} \ (3)$$

$$A_{N,P} = \ A_N + \ A_P \ (4)$$

Thus, $A_{N,P}$ is the total amplitude of the nodal/perigean modulations in each tidal constituent. We also compute the statistical significance of the nodal/perigean modulations in the tidal constituents by estimating the 90% confidence interval of each parameter in Equation 1.

1. **Probability distribution of sea levels**

Following Baranes et al. (2020), we use the quasi-nonstationary skew surge joint-probability method (qn-SSJPM) to derive the probability distribution of sea levels (i.e., the sum of the astronomical tide and skew surge above annual mean sea level). The qn-SSJPM method fits separate probability distributions to skew

surge and the astronomical tide and convolves the two to obtain the joint sea level distribution. The probability distribution function is obtained separately for extreme and non-extreme skew surge events. In the present study, we define extreme events as those above the 0.997^{th} percentile calculated at each station (similar thresholds were chosen in past studies: Arns et al., 2013; Baranes et al., 2020; Menéndez & Woodworth, 2010). We derive the empirical probability for the non-extreme skew surge values through the Weibull formula (Equation 5):

$$\widetilde{F}_{\text{SS}}(x_i) = \frac{i}{n+1} \quad (5)$$

where x_i is the ith-largest skew surge and n the total number of skew surges. For values above the threshold, a Generalized Pareto Distribution (GPD) is fitted to represent the upper tail of the distribution (Equation 6):

$$G_{\text{ss}}(x) = 1 - \left(1 + \xi\frac{x-\mu}{\sigma}\right)^{-1/\xi} \quad (6)$$

where ξ (0) and σ (>0) are the shape and scale parameters, respectively, and μ is the threshold. The cumulative distribution function of all skew surges $F_{\text{ss}}(x)$ is

$$F_{\text{ss}}(x) = \begin{cases} \widetilde{F}_{\text{SS}}(x), & \&x < \mu \\ (1-0.997) * G_{\text{ss}}(x) \ + \ 0.997, & \&x \geq \mu \end{cases} \quad (7)$$

The probability distribution of sea levels (F_{SL}) is calculated by computing the joint probability of the resulting skew surge distribution function and the predicted astronomical tide (Equation 8). Thus, we assume that the skew surge is independent of the tidal cycle, which, although not always the case, they have been shown to be independent in many coastal locations in past studies (Baranes et al., 2020; Batstone et al., 2013; Santamaria-Aguilar and Vafeidis, 2018; Williams et al., 2016). The distribution function for the maximum sea level within a tidal cycle is,

$$F_{\text{SL}}(z) = \left[\Pi_{t=1}^{M} F_{\text{SS}}(z - P_t)\right]^{1/M} \quad (8)$$

where z is the sea level, P_t is the peak astronomical tide level at each cycle t, M is the total number of peak astronomical tide levels, and F_{SS} is the cumulative distribution function of all skew surges. Tides are convolved with 1,000 skew surge GPDs and the 50^{th} quantile of the resulting 1,000 sea levels are used to calculate the annual exceedances.

To satisfy the assumption of independence between extreme sea level events, we apply the extremal index ($\theta(z)$) to each sea level time series, thus removing the possible clustering of high sea levels corresponding to a single extreme event. As pointed out in Batstone et al. (2013), if this dependence between high sea levels is not accounted for, the return period of extreme events could be overestimated. Following Ferro and Segers (2003) and Baranes et al. (2020), the extremal index is the inverse of the mean cluster size:

$$\frac{1}{\theta_0(z)} = \frac{2\left[\sum_{i=1}^{N-1}(I_i - 1)\right]^2}{(N-1) * \sum_{i}^{N-1}[(I_i - 1) * (I_i - 2)]} \quad (9)$$

where N is the number of measured sea levels exceeding z, and I is the inter-exceedance time. The inter-exceedance time varies with the sea level time series and it is defined as the time difference between each value above the threshold. Thus, $\theta = 1$ when there is no clustering in the time series and $\theta < 1$ otherwise. We use the top 3000 high sea levels (z) as thresholds to calculate the extremal index at each tide gauge. Results are then fitted through a least-square regression method to the form:

$$\theta(z) = 1 + a * e^{-(b*z)} \quad (10)$$

In the present paper, we focus on the annual extreme sea level corresponding to a 100-year return period (hereinafter, 100-ESL), i.e., 1% annual chance. The return period of extreme sea levels $T(z)$ is calculated as

$$T(z) = (\theta(z) * N * [1 - F_{\mathrm{SL}}(z)])^{-1} \quad (11)$$

1. **Nodal and perigean modulations in extreme sea levles**

The annual 100-ESL resulting from the qn-SSJPM are stored at each station. As in Section 3.2, we estimate the tidally-induced changes in the 100-ESL through a least-squares regression model to estimate the harmonic parameters of the nodal and perigean cycles. The amplitudes of the nodal/perigean modulations and their subharmonics are estimated using 18.61-, 9.305-, 8.85-, 4.425-year periods. The amplitudes of the 18.61- and 4.425-year cycles are found to be dominant over the 9.305- and 8.85-year cycles at 87% of sites, in agreement with previous studies (Haigh et al., 2011). In the case of the perigean cycle, this occurs because the 8.85-year cycle of lunar perigee coincides with an equinox (semidiurnal tides), a solstice (diurnal tides), or somewhere in between twice during its cycle, thus influencing high water levels as a quasi 4.4-year cycle (Haigh et al., 2011; Pugh and Woodworth, 2014; Ray and Foster, 2016). A more comprehensive explanation of the 4.4-year modulation in high water levels can be found in Ray and Merrifield (2019). On the other hand, the 9.305-year cycle results from the coincidence of the moon's descending node and the equinox (Wood, 2001). However, and in agreement with our results, the influence of the 9.305-year cycle on water levels has been shown to be negligible in previous studies (Amin, 1993; Haigh et al., 2011; Ray, 2007). Therefore, only the 18.61 and 4.4-year modulations of the 100-ESL time series are considered:

$$H_{100-ESL}(t) = \beta_{100-ESL,0} + \beta_{100-ESL,1}(t) + \beta_{100-ESL,2}\cos\left(t * \tfrac{2\pi}{18.61}\right) + \beta_{100-ESL,3}\sin\left(t * \tfrac{2\pi}{18.61}\right) + \beta_{100-ESL,4}\cos\left(t * \tfrac{2\pi}{4.4}\right) + \beta_{100-ESL,5}\sin\left(t * \tfrac{2\pi}{4.4}\right) \quad (12)$$

The amplitude of the nodal/perigean modulations in 100-ESL ($A_{100-ESL,N,P}$) is computed as:

$$A_{100-ESL,N} = \sqrt{\beta^2_{100-ESL,2} + \beta^2_{100-ESL,3}} \quad (13)$$

$$A_{100-ESL,P} = \sqrt{\beta^2_{100-ESL,4} + \beta^2_{100-ESL,5}} \quad (14)$$

$$A_{100-ESL,N,P} = A_{100-ESL,N} + A_{100-ESL,P} \quad (15)$$

$$\overline{B}_{100-ESL} = \beta_{100-ESL,0} + \beta_{100-ESL,1}\bar{t} \quad (16)$$

The average 100-ESL ($\overline{B}_{100-ESL}$) is then combined with the nodal and perigean amplitudes to assess the tidally-induced changes in flood hazard during a crest ($\overline{B}_{100-ESL} + A_{100-ESL,N,P}$) and a trough ($\overline{B}_{100-ESL} - A_{100-ESL,N,P}$) of the nodal/perigean cycle. The statistical significance of the nodal/perigean modulations in 100-ESL is assessed by computing the 0.90 confidence interval of each parameter in Equation 12.

The relative importance of the two cycles in modulating 100-ESL is calculated as the ratio of the amplitude of the nodal modulation in 100-ESL to the combined amplitude of nodal and perigean modulations:

$$\frac{A_{100-ESL,N}}{A_{100-ESL,N}+A_{100-ESL,P}} \quad (17)$$

1. **Mapping flood hazard**

Changes in the flood extension derived from the tidally-induced variations in extreme sea levels are estimated in the four study cases (Section 2.2). We map the area inundated by the water level corresponding to the variation of the 100-ESL due to the nodal/perigean cycles (Section 3.4). We use a static inundation approach in which areas hydraulically connected with the sea and below a specific water level are considered flooded. The statistic inundation method is developed in MATLAB by making use of a preprocessing image software package. Thus, we can identify the hydrologic connections with the sea and the extension of the flooded areas under different water levels with a low computational cost.

The methodology is based on the identification and delimitation of all independent polygons present in a two-dimensional grid. We convert the positive (land) and negative (water) values in the DEM into a mask of zeros and ones, respectively, transforming the DEM into a black and white image. We then apply the image preprocessing software to find all polygons included in the grid and identify those areas connected to the sea (i.e., included in the polygon defined as "sea"). The flooded area is obtained as the difference between the area of the "sea-polygon" under non-flooding conditions (i.e., the original DEM) and the area of the "sea-polygon" obtained after inundating the DEM (reducing the elevations by a specific water level).

We acknowledge that dynamic inundation models, if run at sufficiently high resolution to resolve urban infrastructure, could produce more accurate absolute results in terms of the flood extent, but our focus here is on assessing the differences when using two 100-ESL values modulated only by long-period tidal fluctuations. Hence the simplistic but computationally more efficient static approach is preferred.

1. **Results**

   (a) **Nodal and perigean amplitudes in tidal constituents**

The amplitudes of the nodal/perigean modulations in the five tidal constituents (K_1, M_2, N_2, O_1, and S_2) are shown in Figure 1 for the tide gauges where the amplitude is significant. Note that the nodal/perigean modulations can be statistically insignificant for a specific constituent but significant for other constituents at the same site. We find that the nodal/perigean modulations are significant in the S_2 constituent at 199 out of the 344 tide gauges (Figure 1e). This number is smaller than for the other four tidal constituents (328 gauges for K_1; 325 for M_2; 302 for N_2; and 336 for O_1). On average, the amplitude of the nodal/perigean modulation is largest for M_2 (Figure 1b); this reflects the prevalence of semi-diurnal forcing over much of the world's oceans. The diurnal K_1 and O_1 modulations show the second highest amplitude, overall (Figure 1a and Figure 1d, respectively), and are large in regions with predominant diurnal forcing, such as the Northeast Pacific (especially Alaska) and Southeast Asia. The amplitudes of the nodal/perigean modulations in the five major constituents are consistent with previous studies (Feng et al., 2015; Ray, 2009; Ray and Talke, 2019).

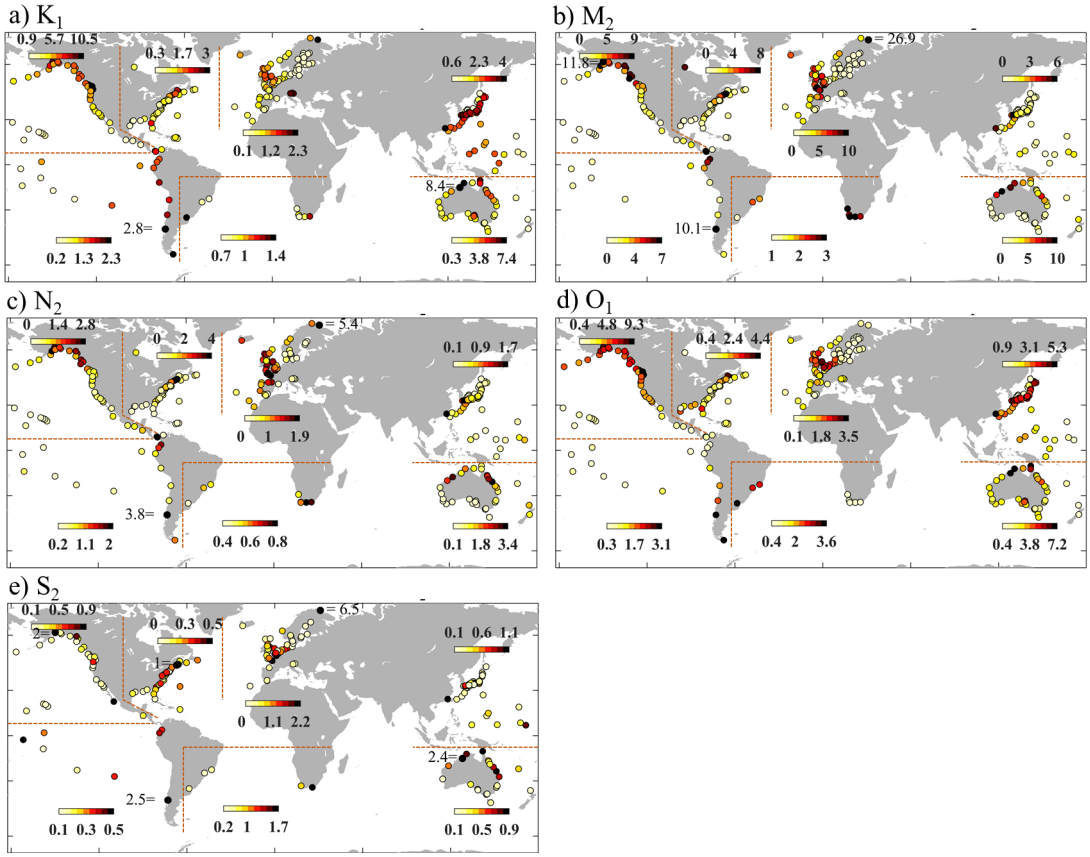

Figure 1. Amplitudes (cm) of nodal/perigean modulations ($A_{N,P}$) in five tidal constituents: a) K_1, b) M_2, c) N_2, d) O_1, and e) S_2. In order to better show

the spatial variability of these modulations, the color bars are specific for seven areas: (1) western and northwestern Pacific, (2) southeastern Indic and southwestern Pacific, (3) southern Atlantic, (4) northeastern Atlantic, (5) southeastern Pacific, (6) northeastern Pacific, and (7) northwestern Atlantic. In addition, for locations with amplitudes much higher than those at the neighboring stations the actual numbers are provided, so that they do not mask the rest of the stations. Sites that are not shown in the figure are locations where the nodal/perigean modulations are not statistically significant.

1. **Tidally-induced changes in 100-ESL**

Next, we consider tidally induced changes in 100-ESL. Figure 2 shows, as an example, the annual (colored lines) and time-averaged (bold dashed black line) sea level exceedance curves for five sites located in areas with different tidal regimes: 1. Fremantle in Australia (diurnal), 2. San Francisco in the U.S. (mixed mainly semidiurnal), 3. Cristobal in Panama (diurnal), 4. Vigo in Spain (semidiurnal), and 5. Nagoya in Japan (mixed mainly semidiurnal). In some areas, such as Fremantle and San Francisco, a secular temporal evolution is clear; most recent return period curves are located above the time-averaged curve, i.e., a particular sea level would have a higher probability of occurrence in recent years. In Figure 2, the annual 100-ESL corresponds to those values falling on the vertical red dashed line.

Figure 3 displays the annual 100-ESL (black lines) as well as the harmonic fitting (red bold line) resulting from Equation 12, for the same five locations shown in Figure 2. Note that the nodal/perigean cycles in 100-ESL in Freemantle, San Francisco, and Cristobal are roughly 180 degrees out of phase with Vigo and Nagoya. The phases of the nodal/perigean signals depend on the form of the tide; based on equilibrium theory, when the nodal modulation of diurnal tides is at a maximum, the nodal modulation of semidiurnal tides is at a minimum (Haigh et al., 2011). Thus, the results for Fremantle, Cristobal, Vigo, and Nagoya agree with the equilibrium theory. San Francisco, however, last peaked in 2008, corresponding with the nodal modulation of diurnal tides. This result reflects the complexity of the mixed semidiurnal tides, particularly in locations with a tidal form factor close to 1.5 (i.e., close to mixed diurnal tides), as is the case in San Francisco. In addition, local differences in the phase of the nodal modulation in high water levels can result from the bathymetry (Peng et al., 2019) and shallow-water interactions between semidiurnal and diurnal constituents (Feng et al., 2015).

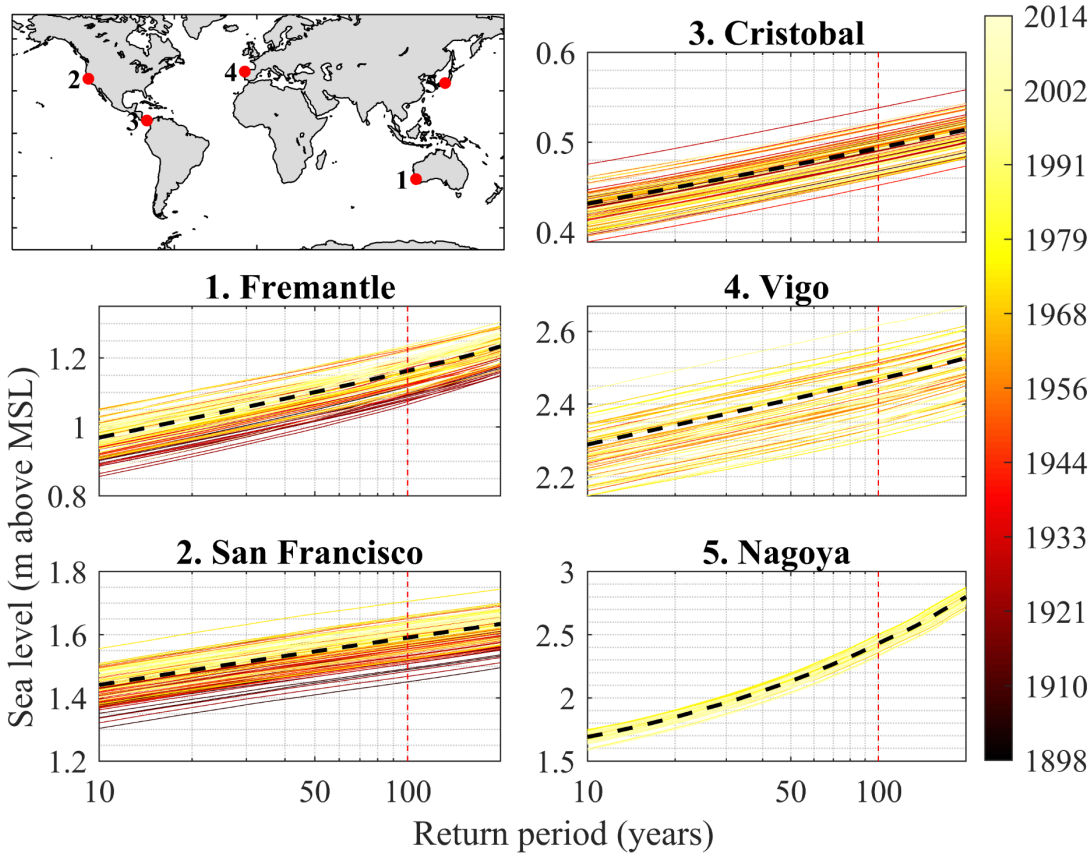

Figure 2. Annual exceedance curves (colored lines) for five locations: 1. Fremantle (Australia), 2. San Francisco (U.S.), 3. Cristobal (Panama), 4. Vigo (Spain), and 5. Nagoya (Japan). The annual exceedance curve for the full period is shown as a dashed black bold line. The annual 100-ESL are the values falling on the red dashed line.

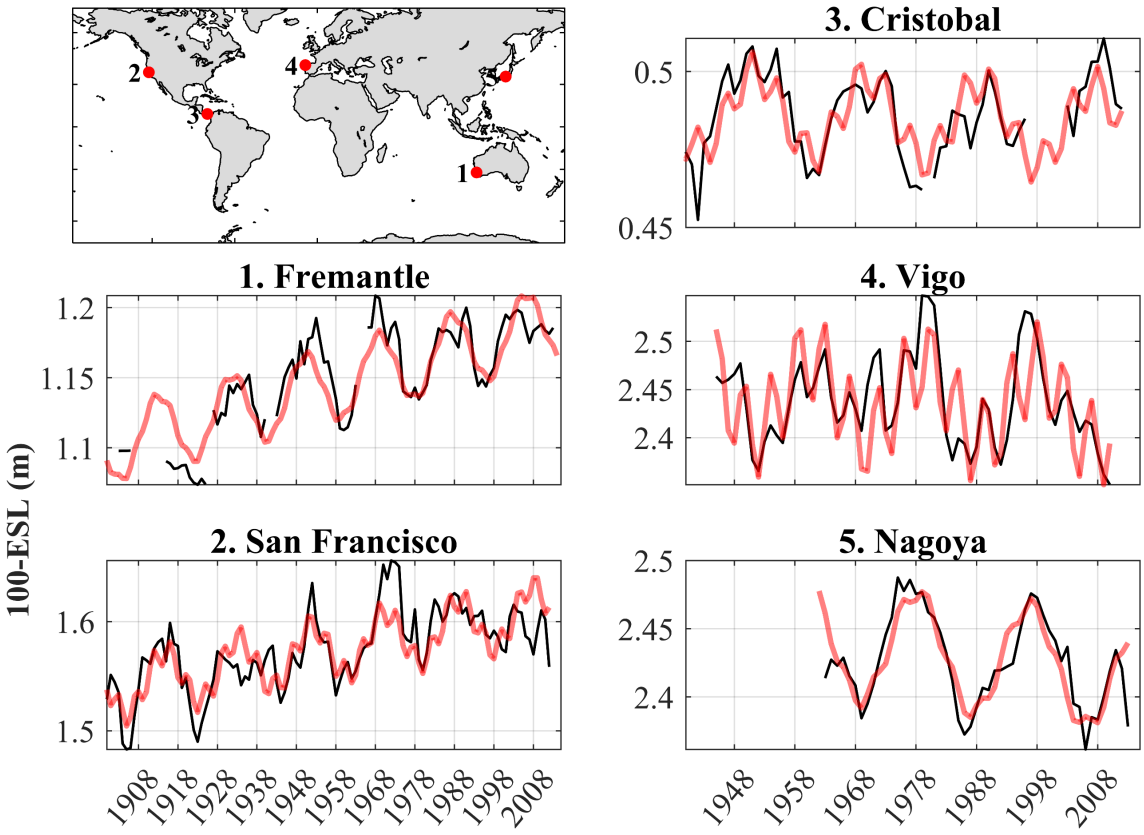

Figure 3. Annual 100-ESL (black line) and the harmonic analysis using 18.61 and 4.4-year periods (red bold lines) for five sites located in different tide regimes: 1. Fremantle (Australia, diurnal tides), 2. San Francisco (U.S., mixed mainly semidiurnal tides), 3. Cristobal (Panama, diurnal tides), 4. Vigo (Spain, semidiurnal tides), and 5. Nagoya (Japan, mixed mainly semidiurnal tides).

The nodal/perigean modulations in 100-ESL significantly increase the flood hazard during their positive phases and peaks. Identifying the timing of these peaks can help prepare for and mitigate coastal flood risk. Figure 4a shows the absolute value of the time difference (in years) between the year 2021 and the closest peak of the nodal/perigean modulations. Note that the peak could occur before or after 2021. Only sites where the nodal/perigean modulations in 100-ESL are significant are shown. In general, there is regional coherence in the timing of peak nodal/perigean modulations in 100-ESL. However, some discrepancies are observed in northwestern Australia, the Gulf of Mexico, and the west coast of Canada. Locations that will peak after 2021 (the vast majority) are currently in a positive phase of the modulation and therefore at a higher risk of flooding. Locations that peaked before 2021 are in a negative phase of the nodal/perigean

modulation in 100-ESL.

Figure 4b shows the year of the next expected peak of the nodal/perigean cycles across the stations. Note that, abrupt color changes between neighboring sites in Figure 4b, do not indicate great variations in the timing of the nodal/perigean peak; in some areas (e.g., in Australia), the next peak at one station is in ~18.6 years because it peaked very recently or is peaking now (in 2021), while at other near station it hasn't happened yet but will do so very soon (sites peaking in 2021 are light diamonds in Figure 4a, which become black dots in Figure 4b). The nodal/perigean modulations are currently peaking at some places located in southern Australia, Hawaii, the eastern coast of Florida, Puerto Rico, southern Alaska, and the western coast of Canada.

Thompson et al. (2021) studied the influence of the 18.6-year nodal cycle in the frequency of high-tide flooding along the U.S. coast, identifying a pronounced inflection before mid-century. Our results mainly agree with theirs; the next peak of the nodal/perigean modulations in 100-ESL is expected to occur before mid-century in most sites along the U.S. coast (Figure 4b). However, some differences are found as a result of the inclusion of the 4.4-year perigean cycle in our analysis. For example, Thompson et al. (2021) showed that the nodal cycle peaks just before 2024 in St Petersburg (western Florida) while our results indicate that the nodal/perigean modulations in 100-ESL are peaking now (in 2021). While the 4.4-year cycle contribution to the total amplitude in St Petersburg is relatively small (~20%, Figure 6) it still influences the timing of the long-term tidal modulations in 100-ESL. A higher influence on the timing of the peak can be expected in areas strongly influenced by the perigean cycle.

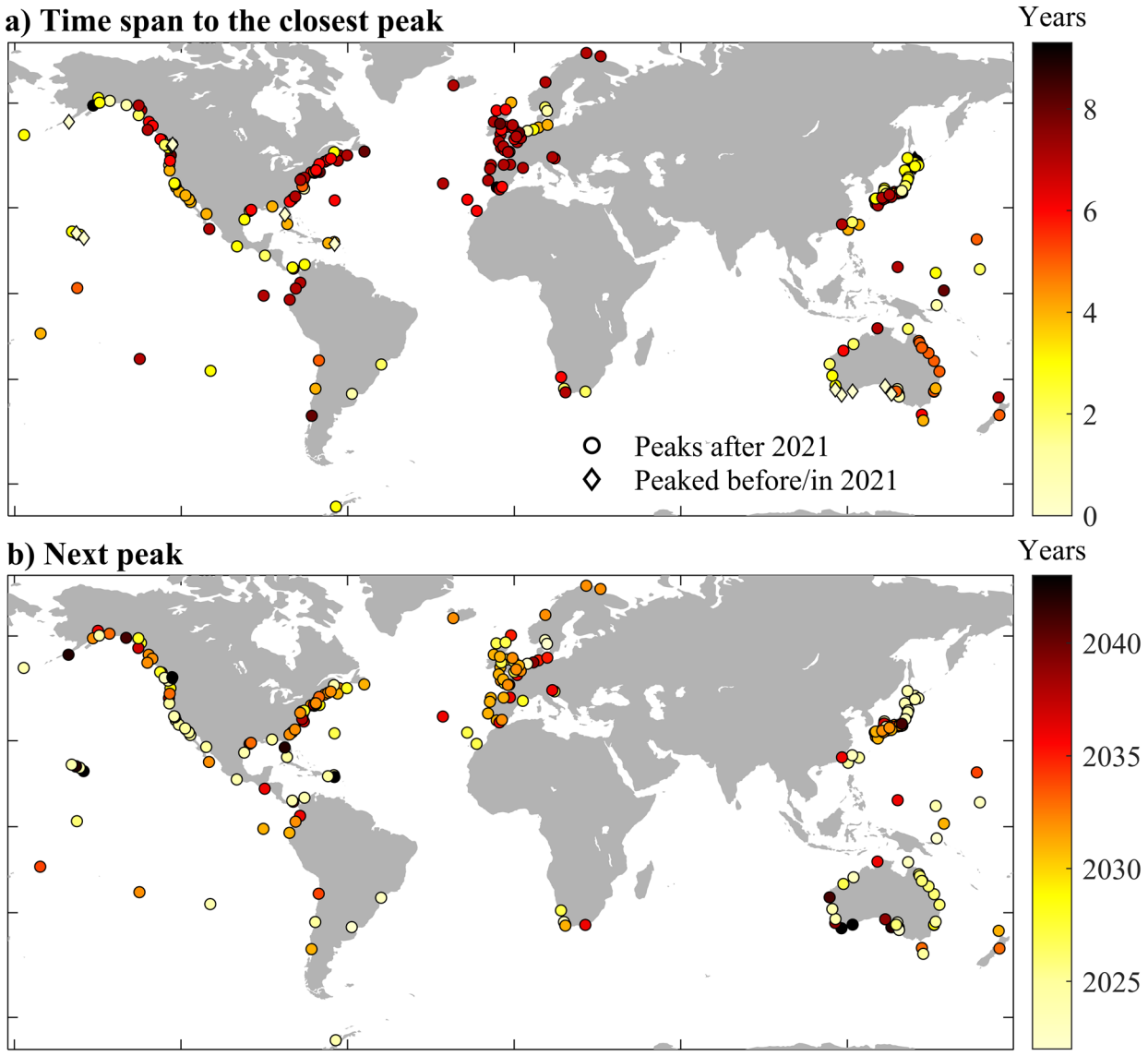

Figure 4. a) Time difference in years between the closest peak of the nodal/perigean modulations in 100-ESL and the year 2021. Diamonds indicate sites where the nodal/perigean modulation peaked before and in 2021 while circles show places where the modulation peaks after 2021. b) Timing (in years) of the next peak of the nodal/perigean cycles. Tide gauges where the nodal/perigean modulations in 100-ESL are statistically insignificant are not

included in the figure.

The amplitudes of the nodal/perigean modulations in 100-ESL ($A_{100-ESL,N,P}$), are plotted for all stations in Figure 5. We find a statistically significant nodal/perigean signal in 100-ESL at 234 of the 344 tide gauges (68%). The maximum influence of the nodal/perigean signal is located in western France, where it can increase/decrease the 100-ESL by ~22 cm. The nodal/perigean modulation is also relevant in the eastern coast of China (~13cm), northwestern and northeastern coasts of Australia (~18cm), the Pacific coast of Panama (~18cm), and southern Alaska (~14cm). As expected, areas with higher influence of the nodal/perigean cycles in 100-ESL overlap with areas where the nodal/perigean modulations are also important in the tidal constituents (Figure 1). On the other hand, tide gauges with statistically insignificant nodal/perigean 100-ESL modulations are located mainly in the Baltic Sea and the Gulf of Bothnia, where tides are small (Medvedev et al., 2013, 2016). Results agree with the small nodal/perigean modulations found in the five tide constituents in the Baltic Sea and the Gulf of Bothnia (Figure 1).

Although the results are not directly comparable due to differences in defining extreme water levels and in the methodology, the spatial patterns of the nodal/perigean modulations in 100-ESL agree with those found in monthly mean high water levels by Peng et al. (2019). These authors used water level records from tide gauges located along the global coasts. Similar to what we show here, Peng et al. (2019) found a strong effect of the nodal cycle on the Bay of Fundy, Gulf of Alaska, Panama and southern Chile. They also found a strong influence of the nodal signal in the Gulf of Tonkin; however, we don't have tide gauges in that area due to our data selection criteria. In Europe, Peng et al. (2019) showed that the amplitude of the nodal/perigean signals in the monthly mean high water levels was large (compared to the neighboring sites) in the Bristol area and the English channel. Unlike them, our results show that the amplitudes of the nodal/perigean modulations in 100-ESL are also large in many other tide gauges located along the west coast of Europe, mainly the western coast of France and the northern coast of Spain. In Australia, Peng et al. (2019) found a large nodal influence on the northwestern coast while we also find a high amplitude of the nodal/perigean modulations along the northeastern coast. One noticeable difference is found in South Africa, where we find a higher amplitude of the nodal/perigean modulations in 100-ESL.

An interesting result is the nodal/perigean signals at the Wyndham tide gauge (northwestern Australia). The amplitude of the signal is very strong in the M_2, K_1, O_1, and S_2 tidal constituents, in comparison to the neighboring tide gauges. However, the long-term tidal modulation is not present in 100-ESL at a 90% confidence level, while it is significant at the neighboring tide gauges. Further research is required to characterize the nodal/perigean cycles in extreme sea levels at this location.

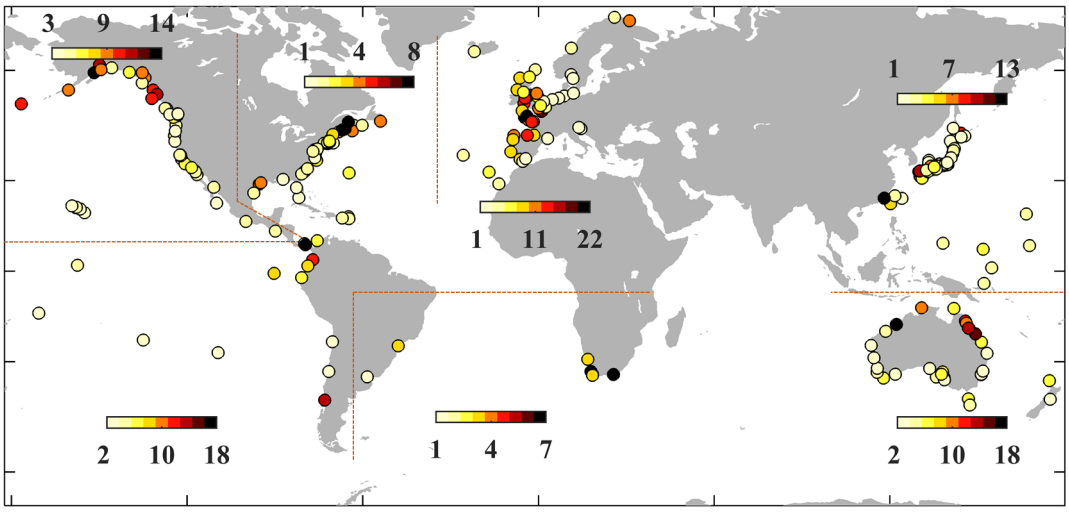

Figure 5. Amplitude (cm) of the nodal/perigean modulations in 100-ESL ($A_{100-ESL,N,P}$). The color bars change across seven regions to better show the spatial variability in the tidally-induced changes in 100-ESL. Tide gauges where the nodal/perigean modulations in 100-ESL are statistically insignificant are not included in the figure.

We also analyze the relative importance of the two cycles in modulating 100-ESL by calculating the relative contribution of the nodal cycle to the total amplitude of the nodal/perigean signals (Equation 17, Section 3.4). Our results (Figure 6) show spatial coherence across sites and a general agreement with the diurnal and semidiurnal spatial pattern of tides (Figure 8 in Haigh et al., 2011). Note that, although there is a general tendency that the perigean cycle influences sea levels in semidiurnal tidal zones and the nodal cycle influences sea levels in diurnal tides zones, both modulations may be present for either tidal regime (Haigh et al., 2011). In Europe, there are two distinguishable areas; the nodal modulation in 100-ESL is more prominent in the Mediterranean Sea, the North Sea, and along the west and north coasts of Norway. Results for the North Sea and Norway contrast with the tidal regime, which is predominately semidiurnal. However, in the case of the North Sea, results are consistent with the strong modulation of the nodal/perigean cycles in the diurnal O_1 tidal constituent (Figure 1d).

Along the rest of the European coast, the perigean modulation is predominant in the 100-ESL, with the exception of the Holyhear tide gauge, located on the western coast of the UK. The coasts of Japan also show spatial coherence in the nodal/perigean modulations in 100-ESL, with two clusters; the northern coast is dominated by the nodal signal while the perigean signal is more relevant in the south. The nodal modulation is again more predominant along the coast of

Taiwan and its surroundings with the exception of Xiamen in China. Smaller spatial coherent clusters are found along the coasts of Australia although the southern coast is predominantly influenced by the nodal cycle while the perigean is more important in the north. Overall, the nodal cycle is the predominant modulation in 100-ESL on the eastern coast of the U.S. and Canada but the perigean modulation becomes relevant in some scattered places, showing a perigean contribution of 50 to 70% to the total amplitude.

Modulations by both cycles are slightly more even in magnitude along the southeast coast of the U.S. The nodal modulation is more important than the perigean on the Pacific coast of Mexico, while the perigean cycle is, overall, more prominent at northern latitudes, from Washington up to Alaska (U.S.). The spatial coherence of the long-term tidal signal in 100-ESL is more difficult to assess in South Africa, South America, and the Pacific islands due to the scattered locations where the nodal/perigean modulations are statistically significant in 100-ESL.

The spatial clusters of the relative importance of the two cycles in modulating 100-ESL (Figure 6) mostly agree with the clusters found in the timing of the peak of the modulation (Figure 4a). For example, sites in Japan with a high nodal influence will peak in ~2-3 years, while sites on the southern coast mainly influenced by the perigean cycle will peak in ~7-8 years. Similar patterns are found in Australia, Taiwan and China, Europe, and to a lesser extent, the northwestern coast of the U.S. and Canada.

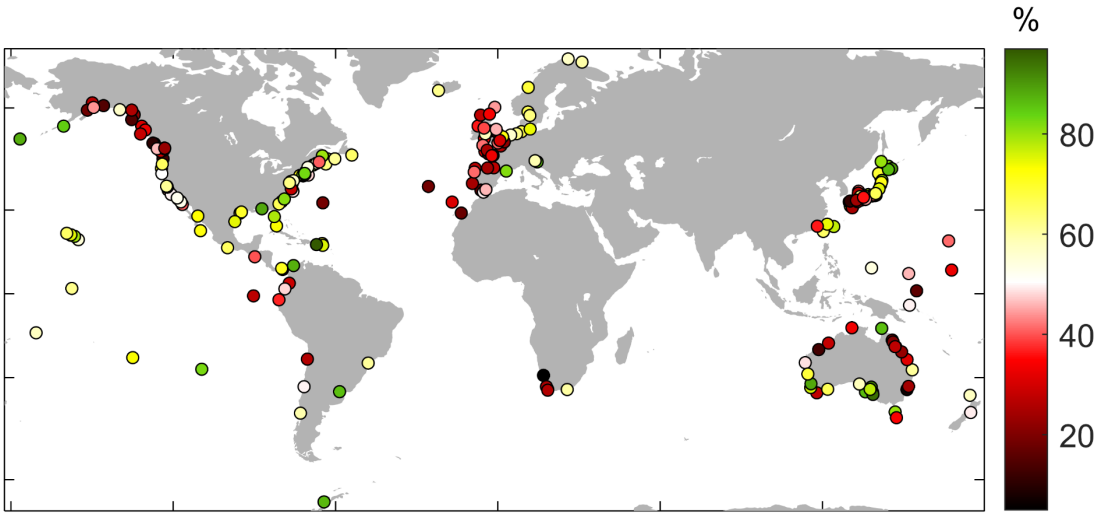

Figure 6. Relative importance (in %) of the nodal signal to the total amplitude of the nodal/perigean modulations in 100-ESL at sites where the overall amplitude is significant. Green-yellow colors indicate a higher influence of the 18.6-year nodal signal while black-red colors indicate a higher influence of the 4.4-year

perigean signal in 100-ESL. White color represents an equal presence of both cycles (50%).

1. **Influence of nodal/perigean 100-ESL modulations in inundation modeling**

Finally, we evaluate the impact of the nodal/perigean modulations in 100-ESL on the estimated flood extent of a 100-year event, for four case study sites. This is quantified by deriving 100-ESL under a positive and negative phase of the modulation (Section 3.4) in Boston, Miami, South San Francisco Bay, and Santa Barbara. Table 2 shows the area covered by the DEM used for each case study, the range of the nodal/perigean modulations in 100-ESL found in the closest tide gauge to each site, and the ratio of the area flooded under a peak and a trough of the modulation (F, in % of change). As an example, the variation in the flood area derived from the nodal/perigean modulations in 100-ESL is shown for San Francisco Bay (Figure 7).

Results show that changes in 100-ESL derived from long-term tidal variations lead to differences in potential flood extents of up to ~45% in Boston. This is almost four times the relative contribution of mean sea-level rise (0.82 m under an RCP8.5 scenario by 2100, relative to the period of 1986-2005, IPCC, 2013) to the area vulnerable to flooding under a category 3 storm on the coast of Massachusetts (12.2%, Figure 4 in Maloney and Preston, 2014). Changes for the other locations are smaller; 12.9% in South San Francisco Bay, 6% in Santa Barbara, and 11% in Miami. Differences among sites arise from the variation in characteristics of each area, including the amplitude of the nodal/perigean amplitudes in 100-ESL and the steepness of the coastal topography. For example, tidal constituents are small in Miami (M_2 ~ 0.3m) and the nodal cycle is not prominent (Haigh et al., 2011). The difference between Santa Barbara and San Francisco, both in California with similar mixed, semidiurnal forcing, demonstrates the influence of local variations. The greater potential inundation in South San Francisco Bay is likely attributable both to generally steeper topography in Santa Barbara (see also Barnard et al., 2019). Note that the flood areas are zones below the 100-ESL elevation and hydraulically connected to the sea according to the DEM; however, the actual inundation area is also affected by flood pathways, drainage, pumps, and other civil infrastructure, which are not accounted for here.

Table 2. The area flooded (km^2) by 100-ESL under a positive and negative nodal/perigean cycle. The first column depicts the area over which the flood mapping analysis is performed. The range (cm) of the nodal/perigean modulations in 100-ESL is shown in the second column. The ratio between the area flooded under a positive and negative phase is shown in the last column (F, in % of change).

	Study area (km^2)	**Range of nodal/perigee modulations in 100-ESL (cr**
Boston	98.3	10.5

	Study area (km^2)	Range of nodal/perigee modulations in 100-ESL (cr
South San Francisco Bay	2,435	7.9
Santa Barbara	178.2	12.4
Miami	330	3.1

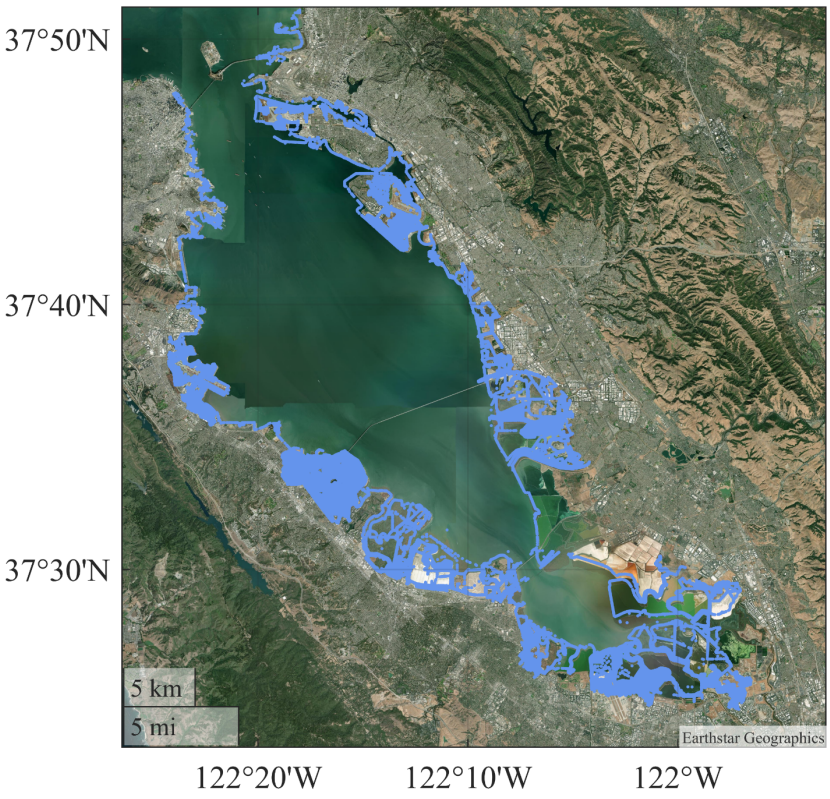

Figure 7. Tidally driven variations in flood extent in South San Francisco Bay. Note that this is not the total flood area but the difference in the area flooded by a 100-ESL event occurring under a peak and a trough of the nodal/perigean cycles.

4. Conclusions

In this paper, we have assessed the nodal/perigean modulations in five major tidal constituents (K_1, M_2, N_2, O_1, and S_2) at 344 tide gauges located along the global coasts. In agreement with the equilibrium theory, the amplitudes of the nodal/perigean modulations are higher in the M_2 tidal constituent at most

sites, reaching up to 10 cm in Europe. The amplitudes of the nodal/perigean modulations are also large in K_1 and O_1, particularly along the western coast of the U.S. and Canada, and northern Australia. Although the number of sites where the nodal/perigean modulations are present in S_2 is lower than for the other four tidal constituents, the nodal/perigean modulations in S_2 are statistically significant at 199 out of the 344 tide gauges.

We have used the qn-SSJPM to estimate the annual sea level exceedance curves, retaining the long-term astronomical tide modulations and thus allowing us to assess the influence of long-term tides on the 100-year return sea level (100-ESL). Our results show that the nodal/perigean modulations impact the flood hazard on interannual to decadal time scales at 234 tide gauges. This number is consistent with previous works that assessed the nodal and perigean modulations in observed monthly high water levels (Peng et al., 2019). We have found some exceptions where the nodal/perigean influence in the five major tidal constituents is strong, but it vanishes when analyzing the effect on 100-ESL. This is especially noticeable in Wyndham (northwestern Australia).

The amplitude of the nodal/perigean modulations in 100-ESL greatly varies across stations, reaching up to 22 cm in western France. Other places with high amplitude of the nodal/perigean modulations in 100-ESL are found in the eastern coast of Europe, the eastern coast of China, the northwestern and northeastern coasts of Australia, southern Alaska, and the Pacific coast of Panama. Further research is needed to assess the changes in the amplitude of the nodal/perigean modulations in extreme sea levels at lower return periods, as opposed to the 100-year return levels we focused on in the present study.

Identifying the years at higher risk of flooding due to the nodal/perigean modulations in extreme water levels can help coastal risk management. We have detected the year of the next expected peak of the nodal/perigean cycles across the stations. Some examples of places where the nodal/perigean modulations are currently peaking, or are expected to peak relatively soon, are located in northern Japan, southern Australia, Hawaii, and the eastern coast of Florida. In this line, we have identified a regional coherence in the timing of the peak of the nodal/perigean modulations in 100-ESL.

We have assessed the relative contribution of the nodal versus perigean cycles to the total amplitude of the modulation in 100-ESL. Overall, results show spatial similarities and a general agreement with the prevailing tidal regime. We have found that the timing of the peak of the modulation is highly correlated with which signal (nodal or perigee) predominates at each site, highlighting the importance of accounting for both cycles when assessing the timing of the nodal/perigean peak modulations.

The tidally-induced changes in 100-ESL also affect estimates of the flood surface area. We have found that nodal/perigean modulations in 100-ESL can lead to changes in the area of the 100-year flood area of up to ~45%, for example in Boston, U.S. The changes in flood area caused by long-term changes in

tides vary with the steepness of coastal topography and the amplitude of the nodal/perigean modulations in 100-ESL.

In the present study, we have shown that the nodal/perigean modulations influence low-frequency events (100-year return level) along the global coasts, leading to important variations in flood hazard and potentially flooded surface area. Although further research is required to assess the influence of the tidally-induced changes in flood hazard maps in specific study areas, our results highlight the importance of integrating these tidally-induced and predictable changes in 100-ESL into coastal vulnerability assessments and adaptation plans.

Acknowledgments

We thank GESLA-2 (http://www.gesla.org/) for providing tide gauge datasets and Hannah Baranes for making the qn-SSJPM code available (https://zenodo.org/record/3898657). This work was funded by NSF PREEVENTS award numbers 1854896, 94267271, and 2013280. SAT was also funded by the National Science Foundation Award number 1455350.

References

Amin, M.: Changing mean sea level and tidal constants on the west coast of australia, Mar. Freshw. Res., 44(6), 911–925, doi:10.1071/MF9930911, 1993.Arns, A., Wahl, T., Haigh, I. D., Jensen, J. and Pattiaratchi, C.: Estimating extreme water level probabilities: A comparison of the direct methods and recommendations for best practise, Coast. Eng., 81, 51–66, doi:10.1016/j.coastaleng.2013.07.003, 2013.Baranes, H. E., Woodruff, J. D., Talke, S. A., Kopp, R. E., Ray, R. D. and DeConto, R. M.: Tidally Driven Interannual Variation in Extreme Sea Level Frequencies in the Gulf of Maine, J. Geophys. Res. Ocean., 125(10), doi:10.1029/2020JC016291, 2020.Barnard, P. L., Erikson, L. H., Foxgrover, A. C., Hart, J. A. F., Limber, P., O'Neill, A. C., van Ormondt, M., Vitousek, S., Wood, N., Hayden, M. K. and Jones, J. M.: Dynamic flood modeling essential to assess the coastal impacts of climate change, Sci. Rep., 9(1), 1–13, doi:10.1038/s41598-019-40742-z, 2019.Batstone, C., Lawless, M., Tawn, J., Horsburgh, K., Blackman, D., McMillan, A., Worth, D., Laeger, S. and Hunt, T.: A UK best-practice approach for extreme sea-level analysis along complex topographic coastlines, Ocean Eng., 71, 28–39, doi:10.1016/j.oceaneng.2013.02.003, 2013.BODC, B. O. D. D.: UK Tide Gauge Network, [online] Available from: https://www.bodc.ac.uk/data/hosted_data_systems/sea_level/uk_tide_gauge_network/, n.d.Caldwell, P. and Merrifield, M.: Joint Archive for Sea Level (JASL). Data Report: October 2015, 2015.Codiga, D. L.: Unified Tidal Analysis and Prediction Using the UTide Matlab Functions, , (September), 59, doi:10.13140/RG.2.1.3761.2008, 2011.Eliot, M.: Influence of interannual tidal modulation on coastal flooding along the Western Australian coast, J. Geophys. Res. Ocean., 115(11), 1–11, doi:10.1029/2010JC006306, 2010.Feng, X., Tsimplis, M. N. and Woodworth, P. L.: Nodal variations and long-term changes in the main tides on the coasts of China, J. Geophys. Res. Ocean., 120(2), 1215–

1232, doi:10.1002/2014JC010312, 2015.Ferro, A. T. C. and Segers, J.: Inference for Clusters of Extreme Values, R. Stat. Soc., 65(2), 545–556, 2003.Flavelle, C., Lu, D., Penney, V., Popovich, N. and Schwartz, J.: New Data Reveals Hidden Flood Risk Across America, New York Times, 29th June [online] Available from: https://www.nytimes.com/interactive/2020/06/29/climate/hidden-flood-risk-maps.html, 2020.Gall, M., Borden, K. A., Emrich, C. T. and Cutter, S. L.: The unsustainable trend of natural hazard losses in the United States, Sustainability, 3(11), 2157–2181, doi:10.3390/su3112157, 2011.Gesch, D., Palaseanu-Lovejoy, M., Danielson, J., Fletcher, C., Kottermair, M., Barbee, M. and Jalandoni, A.: Inundation exposure assessment for majuro atoll, republic of the Marshall islands using a high-accuracy digital elevation model, Remote Sens., 12(1), doi:10.3390/rs12010154, 2020.Haigh, I. D., Eliot, M. and Pattiaratchi, C.: Global influences of the 18.61 year nodal cycle and 8.85 year cycle of lunar perigee on high tidal levels, J. Geophys. Res. Ocean., 116(6), 1–16, doi:10.1029/2010JC006645, 2011.IPCC: Climate Change 2013: The Physical Science Basis, Contribution ofWorking Group I to the Fifth Assessment Report of the Intergovernmental Panel on Climate Change, Cambridge University Press. [online] Available from: http://www.climatechange2013.org/report/full-report/, 2013.JMA, J. M. A.: Japan Meteorological Agency, [online] Available from: http://www.jma.go.jp/jma/indexe.html, n.d.Kron, W.: Coasts: The high-risk areas of the world, Nat. Hazards, 66(3), 1363–1382, doi:10.1007/s11069-012-0215-4, 2013.Li, S., Wahl, T., Talke, S. A., Jay, D. A., Orton, P. M., Liang, X., Wang, G. and Liu, L.: Evolving tides aggravate nuisance flooding along the U.S. coastline, Sci. Adv., 7(10), 1–10, doi:10.1126/sciadv.abe2412, 2021.Maloney, M. C. and Preston, B. L.: A geospatial dataset for U.S. hurricane storm surge and sea-level rise vulnerability: Development and case study applications, Clim. Risk Manag., 2(July 2014), 26–41, doi:10.1016/j.crm.2014.02.004, 2014.Medvedev, I. P., Rabinovich, A. B. and Kulikov, E. A.: Tidal oscillations in the Baltic Sea, Oceanology, 53(5), 526–538, doi:10.1134/S0001437013050123, 2013.Medvedev, I. P., Rabinovich, A. B. and Kulikov, E. A.: Tides in three enclosed basins: The baltic, black, and caspian seas, Front. Mar. Sci., 3(APR), 1–7, doi:10.3389/fmars.2016.00046, 2016.Menéndez, M. and Woodworth, P. L.: Changes in extreme high water levels based on a quasi-global tide-gauge data set, J. Geophys. Res. Ocean., 115(10), 1–15, doi:10.1029/2009JC005997, 2010.NOAA: Lidar Datasets at NOAA Digital Coast, [online] Available from: https://coast.noaa.gov/htdata/lidar1_z/ (Accessed 24 August 2021), 2021.NOAA: NOAA Tides & Currents, [online] Available from: https://tidesandcurrents.noaa.gov/ (Accessed 22 September 2021), n.d.NTCA, N. T. C. A.: National Operations Centre (NOC) Tidal Unit, [online] Available from: http://www.bom.gov.au/oceanography/projects/ntc/ntc.shtml, n.d.Peng, D., Hill, E. M., Meltzner, A. J. and Switzer, A. D.: Tide Gauge Records Show That the 18.61-Year Nodal Tidal Cycle Can Change High Water Levels by up to 30 cm, J. Geophys. Res. Ocean., 124(1), 736–749, doi:10.1029/2018JC014695, 2019.Preston, B. L.: Local path dependence of U.S. socioeconomic exposure to climate extremes and the vulnerability commitment, Glob. Environ. Chang., 23(4), 719–732, doi:10.1016/j.gloenvcha.2013.02.009,

2013.Pugh, D. and Woodworth, P.: Sea-level science: understanding tides, surges, tsunamis and mean sea-level changes, Cambridge University Press., 2014.Rao, A. D., Upadhaya, P., Ali, H., Pandey, S. and Warrier, V.: Coastal inundation due to tropical cyclones along the east coast of India: an influence of climate change impact, Nat. Hazards, 101(1), 39–57, doi:10.1007/s11069-020-03861-9, 2020.Ray, R. and Foster, G.: Future nuisance flooding at Boston caused by astronomical tides alone, Earth's Futur., 4(12), 578–587, doi:10.1002/2016EF000423, 2016.Ray, R. D.: Decadal climate variability: Is there a tidal connection?, J. Clim., 20(14), 3542–3560, doi:10.1175/JCLI4193.1, 2007.Ray, R. D.: Secular changes in the solar semidiurnal tide of the western North Atlantic Ocean, Geophys. Res. Lett., 36(19), 1–5, doi:10.1029/2009GL040217, 2009.Ray, R. D. and Merrifield, M. A.: The Semiannual and 4.4-Year Modulations of Extreme High Tides, J. Geophys. Res. Ocean., 124(8), 5907–5922, doi:10.1029/2019JC015061, 2019.Ray, R. D. and Talke, S. A.: Nineteenth-Century Tides in the Gulf of Maine and Implications for Secular Trends, J. Geophys. Res. Ocean., 124(10), 7046–7067, doi:10.1029/2019JC015277, 2019.Santamaria-Aguilar, S. and Vafeidis, A. T.: Are Extreme Skew Surges Independent of High Water Levels in a Mixed Semidiurnal Tidal Regime?, J. Geophys. Res. Ocean., 123(12), 8877–8886, doi:10.1029/2018JC014282, 2018.Sobey, R. J.: Extreme low and high water levels, Coast. Eng., 52(1), 63–77, doi:10.1016/j.coastaleng.2004.09.003, 2005.Talke, S. A., Kemp, A. C. and Woodruff, J.: Relative Sea Level, Tides, and Extreme Water Levels in Boston Harbor From 1825 to 2018, J. Geophys. Res. Ocean., 123(6), 3895–3914, doi:10.1029/2017JC013645, 2018.Thompson, P. R., Widlansky, M. J., Hamlington, B. D., Merrifield, M. A., Marra, J. J., Mitchum, G. T. and Sweet, W.: Rapid increases and extreme months in projections of United States high-tide flooding, Nat. Clim. Chang., 11(7), 584–590, doi:10.1038/s41558-021-01077-8, 2021.Titus, J. G., Hudgens, D. E., Trescott, D. L., Craghan, M., Nuckols, W. H., Hershner, C. H., Kassakian, J. M., Linn, C. J., Merritt, P. G., McCue, T. M., O'Connell, J. F., Tanski, J. and Wang, J.: State and local governments plan for development of most land vulnerable to rising sea level along the US Atlantic coast, Environ. Res. Lett., 4(4), doi:10.1088/1748-9326/4/4/044008, 2009.Ward, P. J., Marfai, M. A., Yulianto, F., Hizbaron, D. R. and Aerts, J. C. J. H.: Coastal inundation and damage exposure estimation: A case study for Jakarta, Nat. Hazards, 56(3), 899–916, doi:10.1007/s11069-010-9599-1, 2011.Williams, J., Horsburgh, K. J., Williams, J. A. and Proctor, R. N. F.: Tide and skew surge independence: New insights for flood risk, Geophys. Res. Lett., 43(12), 6410–6417, doi:10.1002/2016GL069522, 2016.Wood, F. J.: Tidal Dynamics. Volume I: Theory and Analysis of Tidal Forces., 2001.Woodworth, P. L., Hunter, J. R., Marcos, M., Caldwell, P., Menéndez, M. and Haigh, I.: Towards a global higher-frequency sea level dataset, Geosci. Data J., 3(2), 50–59, 2016.